J Biol Phys (2016) 42:507–524
DOI 10.1007/s10867-016-9419-2

ORIGINAL PAPER

Mode switching of Inositol 1,4,5-trisphosphate receptor channel shapes the Spatiotemporal scales of Ca^{2+} signals

Ghanim Ullah[1] · Aman Ullah[2]

Received: 14 August 2015 / Accepted: 12 April 2016 / Published online: 6 May 2016

Abstract The inositol 1,4,5-trisphosphate ($InsP_3$) receptor ($InsP_3R$) channel is crucial for the generation and modulation of highly specific intracellular Ca^{2+} signals performing numerous functions in animal cells. However, the single channel behavior during Ca^{2+} signals of different spatiotemporal scales is not well understood. To elucidate the correlation between the gating dynamics of single $InsP_3Rs$ and spatiotemporal Ca^{2+} patterns, we simulate a cluster of $InsP_3Rs$ under varying ligand concentrations and extract comprehensive gating statistics of all channels during events of different sizes and durations. Our results show that channels gating predominantly in the low activity mode with negligible occupancy of intermediate and high modes leads to single channel Ca^{2+} release event blips. Increasing occupancies of intermediate and high modes results in events with increasing size. When the channel has more than 50% probability of gating in the intermediate and high modes, the cluster generates very large puffs that would most likely result in global Ca^{2+} signals. The size, duration and frequency of Ca^{2+} signals all increase linearly with the total probability of channel gating in the intermediate and high modes. To our knowledge, this is the first study that quantitatively relates the modal characteristics of $InsP_3R$ to the shaping of different spatiotemporal scales of Ca^{2+} signals.

Keywords Ca^{2+} signaling · Inositol 1,4,5-trisphosphate receptor · Modal gating · Multi-scales

✉ Ghanim Ullah
gullah@usf.edu

[1] Department of Physics, University of South Florida, Tampa, FL 33620, USA

[2] Department of Molecular Neuroscience, Krasnow Institute for Advanced Study, George Mason University, Fairfax, VA 22030, USA

1 Introduction

Cytosolic signals caused by Ca^{2+} released through inositol 1,4,5-trisphosphate ($InsP_3$) receptor ($InsP_3R$) Ca^{2+} channels from the endoplasmic reticulum (ER) regulate numerous cellular functions [1]. The secret of the universality and specificity of Ca^{2+} signals lies in the hierarchy of their dynamics. That is, information is encoded in the spatiotemporal patterning of Ca^{2+} transients. Despite its vital role, the mechanism behind the spatiotemporal patterning of Ca^{2+} signals remains misunderstood.

The $InsP_3R$ is a Ca^{2+} - sensitive Ca^{2+} release channel having a bell-shaped equilibrium open probability (P_o) with respect to Ca^{2+} [2, 3]. It is more probable for the channel to be open in the presence of 2 μM Ca^{2+} on the cytosolic side of the membrane than it is for it to be open at 0.1 μM or 100 μM Ca^{2+}. Opening of $InsP_3R$ also requires the binding of second-messenger $InsP_3$, which is generated in the cytoplasm by the binding of extracellular ligands to the membrane receptors. Patch clamp data on Sf9 cells, an insect cell line derived from the moth *Spodoptera frugiperda*, show that $InsP_3R$ gates in three distinct modes even if the concentrations of Ca^{2+} and $InsP_3$ are kept fixed [4]. The three modes are a low mode with P_o close to zero, an intermediate mode where the channel switches rapidly between closed and open states having $P_o \sim 0.25$, and a high mode with $P_o \sim 0.85$.

$InsP_3Rs$ are distributed in clusters of a few channels per cluster in the membranes of intracellular compartments such as the ER. Experimental observations suggest a simultaneous opening of 6–10 channels during a Ca^{2+} puff (a Ca^{2+} release event caused by a simultaneous opening of more than one channel in a cluster) [5, 6] and a typical cluster diameter of about 0.5 μm [5, 7, 8]. We assume that the maximum number of simultaneously open channels ever observed at a given puff site represents the number of channels within the cluster giving a mean inter-channel spacing of about 100–150 nm depending on the size and number of channels within a cluster.

The Ca^{2+} feedback described above underlies a process of Ca^{2+} - induced Ca^{2+} release (CICR). Ca^{2+} liberation due to CICR may either remain restricted to a single channel opening, giving rise to a blip, cause the simultaneous opening of multiple channels in the cluster to generate a puff, or propagate as a salutatory intracellular Ca^{2+} wave sweeping across multiple clusters. It is this range of signaling patterns that makes Ca^{2+} a universal messenger [1]. Despite the fact that these spatiotemporal scales of Ca^{2+} signals have been the subject of intense research for a number of years, the gating behavior of $InsP_3Rs$ during these scales of Ca^{2+} signals remains misunderstood.

To elucidate the complex spatiotemporal patterning of Ca^{2+} signals generated by $InsP_3Rs$, it is important to link the scales of observations summarized above. We need to understand the behavior of $InsP_3R$ channels during different scales of Ca^{2+} signaling. In this paper, we use a computational framework to investigate the correlation between the gating behavior of $InsP_3R$ with the wide range of statistical properties of elementary Ca^{2+} release events that are the building blocks for Ca^{2+} signaling in many animal cells and explore the behavior of the channel in the spatiotemporal dynamics of Ca^{2+} signaling. We recently employed a data-driven approach to develop a single channel model that can reproduce all observations about $InsP_3R$ including P_o, response of the channel to rapid changes in the ligand concentrations [9] and characteristics of the channel during various modes [10]. We built our cluster model based on this single channel model and extracted comprehensive statistics of the gating properties of all channels during Ca^{2+} signals of different sizes and durations to see how the two correlate with each other.

2 Methods

We modeled the gating of the single $InsP_3R$ channel using the Markov chain shown in Fig. 1 that was originally developed in [10]. This model has 3 open and 9 closed states represented by the letters O and C respectively. The subscript of letter O or C indicates the number of ligands bound to the channel in the state. The first and second indexes respectively in the subscript correspond to the number of Ca^{2+} ions and $InsP_3$ molecules bound to the channel when in the given state. The model also takes into account the modal behavior of the channel. The superscript in each state represents the mode to which the state belongs. The letters L, I and H stand for low, intermediate and high activity mode respectively. Rates between various states are given in Table 1 and the various parameters used in the rates are given in Tables 2 and 3. Notice that some probability flux parameters given in Table 3 are different from those in [10] because here the transition rates $C^L_{20} \rightarrow C^H_{24}$ and $C^L_{20} \leftarrow C^H_{24}$ are assumed to be the same as for $C^L_{00} \rightarrow C^I_{04}$ and $C^L_{00} \leftarrow C^I_{04}$ respectively. Although not required for reproducing puffs, this simplification reduces the total number of parameters by two without qualitatively changing the fits to the data shown in [10]. We direct the interested reader to Ref. [10] for the fits to the single channel data. We also remark that this model successfully reproduces puffs provided that the Ca^{2+} concentration at the channel mouth is high enough (at least 100 μM), which comes naturally from the conversion of the channel current to Ca^{2+} flux (see below) [11, 12].

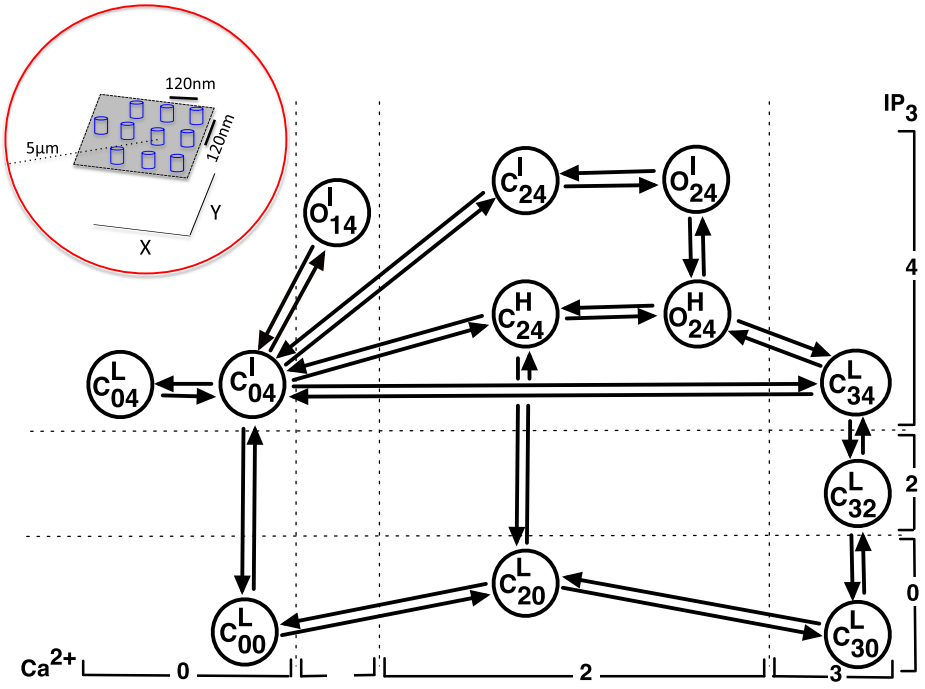

Fig. 1 Kinetic scheme for the single-channel model. The model has nine closed states: C^L_{00}, C^L_{20}, C^L_{30}, C^L_{32}, C^L_{34}, C^L_{04}, C^I_{04}, C^I_{24} and C^H_{24} and three open states: O^I_{14}, O^I_{24} and O^H_{24}. The *inset* shows the channel arrangement inside the cluster (not to scale). The channels are 120 nm apart in the X and Y directions

Table 1 Transition rates between various states

Transition	Rates (ms^{-1})
$C^{I}_{04} \rightarrow C^{H}_{24}$	$rsr(j_{0414}\mathcal{C},\ j_{1424}\mathcal{C}^2)/K_{C^{I}_{04}}$
$C^{I}_{04} \leftarrow C^{H}_{24}$	$rsr(j_{0414}\mathcal{C},\ j_{1424}\mathcal{C}^2)/K_{C^{H}_{24}}\mathcal{C}^2$
$C^{H}_{24} \rightarrow O^{H}_{24}$	$j^{HH}_{2424}/K_{C^{H}_{24}}$
$C^{H}_{24} \leftarrow O^{H}_{24}$	$j^{HH}_{2424}/K_{O^{H}_{24}}$
$O^{H}_{24} \rightarrow C^{L}_{34}$	$j_{2434}\mathcal{C}/K_{O^{H}_{24}}$
$O^{H}_{24} \leftarrow C^{L}_{34}$	$j_{2434}/K_{C^{L}_{34}}$
$C^{I}_{04} \rightarrow C^{L}_{34}$	$rsr(j^{IL}_{0414}\mathcal{C},\ j^{IL}_{1424}\mathcal{C}^2,\ j^{IL}_{2434}\mathcal{C}^3)/K_{C^{I}_{04}}$
$C^{I}_{04} \leftarrow C^{L}_{34}$	$rsr(j^{IL}_{0414}\mathcal{C},\ j^{IL}_{1424}\mathcal{C}^2,\ j^{IL}_{2434}\mathcal{C}^3)/K_{C^{L}_{34}}\mathcal{C}^3$
$C^{I}_{04} \rightarrow O^{I}_{14}$	$j^{II}_{0414}\mathcal{C}/K_{C^{I}_{04}}$
$C^{I}_{04} \leftarrow O^{I}_{14}$	$j^{II}_{0414}/K_{O^{I}_{14}}$
$C^{I}_{24} \rightarrow O^{I}_{24}$	$j^{II}_{2424}/K_{C^{I}_{24}}$
$C^{I}_{24} \leftarrow O^{I}_{24}$	$j^{II}_{2424}/K_{O^{I}_{24}}$
$O^{I}_{24} \rightarrow O^{H}_{24}$	$j_{2424}/K_{O^{I}_{24}}$
$O^{I}_{24} \leftarrow O^{H}_{24}$	$j_{2424}/K_{O^{H}_{24}}$
$C^{I}_{04} \rightarrow C^{L}_{04}$	$j_{0404}/K_{C^{I}_{04}}$
$C^{I}_{04} \leftarrow C^{L}_{04}$	$j_{0404}/K_{C^{L}_{04}}$
$C^{L}_{32} \rightarrow C^{L}_{34}$	$j_{3334}\mathcal{I}^2/K_{C^{L}_{32}}$
$C^{L}_{32} \leftarrow C^{L}_{34}$	$j_{3334}/K_{C^{L}_{34}}$
$C^{L}_{30} \rightarrow C^{L}_{32}$	$j_{3132}\mathcal{I}^2/K_{C^{L}_{30}}$
$C^{L}_{30} \leftarrow C^{L}_{32}$	$j_{3132}/K_{C^{L}_{32}}$
$C^{L}_{20} \rightarrow C^{L}_{30}$	$j_{2030}\mathcal{C}/K_{C^{L}_{20}}$
$C^{L}_{20} \leftarrow C^{L}_{30}$	$j_{2030}/K_{C^{L}_{30}}$
$C^{L}_{00} \rightarrow C^{I}_{04}$	$rsr(j_{0001}\mathcal{I},\ j_{0304}\mathcal{I}^4)$
$C^{L}_{00} \leftarrow C^{I}_{04}$	$rsr(j_{0001},\ j_{0304}\mathcal{I}^3)/K_{C^{I}_{04}}\mathcal{I}^3$
$C^{L}_{20} \rightarrow C^{H}_{24}$	same as that for $C^{L}_{00} \rightarrow C^{I}_{04}$
$C^{L}_{20} \leftarrow C^{H}_{24}$	same as that for $C^{L}_{00} \leftarrow C^{I}_{04}$

rsr is the reciprocal of a sum of reciprocals i.e., $rsr(x_1, x_2, \cdots x_n) \equiv \frac{1}{\sum_{i=1}^{n} \frac{1}{x_i}}$

We placed a single cluster of 10 $InsP_3R$ channels in a planar membrane separated by 120 nm in the X and Y directions (Fig. 1 inset) with each channel at the center of a 5 μm radius sphere. Thus each channel is first individually simulated by placing it at the center of

Table 2 Parameters for occupancies of all states

Parameters	Values
$K_{C^L_{00}}$	1
$K_{C^L_{32}}$	$1.4785 \times 10^7\ \mu M^{-5}$
$K_{C^L_{34}}$	$7.76239 \times 10^7\ \mu M^{-7}$
$K_{O^I_{14}}$	$1.20225 \times 10^8\ \mu M^{-5}$
$K_{C_{04}} = K_{C^L_{04}} + K_{C^I_{04}}$	$2.18267 \times 10^8\ \mu M^{-4}$
$K_{C_{24}} = K_{C^H_{24}} + K_{C^I_{24}}$	$6.1646 \times 10^8\ \mu M^{-6}$
$K_{O_{24}} = K_{O^H_{24}} + K_{O^I_{24}}$	$2.04174 \times 10^9\ \mu M^{-6}$
p	0.8
r	0.95
$K_{C^L_{04}}$	$pK_{C_{04}}$
$K_{C^I_{04}}$	$(1-p)K_{C_{04}}$
$K_{O^H_{24}}$	$rK_{O_{24}}$
$K_{O^I_{24}}$	$(1-r)K_{O_{24}}$
$K_{C^H_{24}}$	$0.5K_{C_{24}}$
$K_{C^I_{24}}$	$(1-0.5)K_{C_{24}}$
$K_{C^L_{20}}$	$K_{C^H_{24}}/K_{C^I_{04}}$
$K_{C^L_{30}}$	$K_{C^L_{34}}/K_{C^I_{04}}$

a 5 μm radius sphere and finally the contributions of all channels to the spatial Ca^{2+} profile of a given channel are computed using the superposition of the individual Ca^{2+} profiles of all channels (see below). The gating of each channel is given by the 12 state model described above. We determined the state of the channel at a given time using a stochastic method described previously [12–14].

Ca^{2+} concentration on the cytoplasmic side of the cluster is controlled by diffusion; the flux coming out from the ER through $InsP_3Rs$, J_j; and the concentrations of free stationary buffers, free mobile buffers and free dye: b_s, b_m and b_d, respectively. Thus the rate equations for Ca^{2+} concentration at distance r_j and time t due to channel j, $c^j(r_j,t)$, and free Ca^{2+} buffers $b_s^j(r_j,t)$, $b_m^j(r_j,t)$, and $b_d^j(r_j,t)$ at distance r_j and time t from channel j are described as:

$$\frac{\partial c^j(r_j,t)}{\partial t} = D_c\nabla_j^2 c^j + J_j + k_s^r(B_s - b_s^j) - k_s^f c^j b_s + k_m^r(B_m - b_m^j) - k_m^f c^j b_m^j + k_d^r(B_d - b_d^j) - k_d^f c^j b_d^j \quad (1)$$

$$\frac{\partial b_s^j}{\partial t} = k_s^r(B_s - b_s^j) - k_s^f c^j b_s^j \quad (2)$$

Table 3 Flux parameters used in the model

Parameters	Pathway	Values
j_{0414}	$C^{I}_{04} \rightleftharpoons C^{H}_{24}$	$5.11487 \times 10^{5}\ \mu M^{-5}\ ms^{-1}$
j_{1424}	$C^{I}_{04} \rightleftharpoons C^{H}_{24}$	$9.88434 \times 10^{6}\ \mu M^{-6}\ ms^{-1}$
j_{2434}	$O^{H}_{24} \rightleftharpoons C^{L}_{34}$	$5.08204 \times 10^{4}\ \mu M^{-7}\ ms^{-1}$
j^{IL}_{0414}	$C^{I}_{04} \rightleftharpoons C^{L}_{34}$	$6.55954 \times 10^{4}\ \mu M^{-5}\ ms^{-1}$
j^{IL}_{1424}	$C^{I}_{04} \rightleftharpoons C^{L}_{34}$	$1.00237 \times 10^{3}\ \mu M^{-6}\ ms^{-1}$
j^{IL}_{2434}	$C^{I}_{04} \rightleftharpoons C^{L}_{34}$	$8.06811 \times 10^{5}\ \mu M^{-7}\ ms^{-1}$
j_{2030}	$C^{L}_{20} \rightleftharpoons C^{L}_{30}$	$8.95522 \times 10^{-3}\ \mu M^{-3}\ ms^{-1}$
j^{II}_{0414}	$C^{I}_{04} \rightleftharpoons O^{I}_{14}$	$2.18273 \times 10^{5}\ \mu M^{-5}\ ms^{-1}$
j^{II}_{2424}	$C^{I}_{24} \rightleftharpoons O^{I}_{24}$	$1.02087 \times 10^{7}\ \mu M^{-7}\ ms^{-1}$
j_{2424}	$O^{I}_{24} \rightleftharpoons O^{H}_{24}$	$7.17650 \times 10^{5}\ \mu M^{-6}\ ms^{-1}$
j_{0404}	$C^{I}_{04} \rightleftharpoons C^{L}_{04}$	$5.76225 \times 10^{4}\ \mu M^{-4}\ ms^{-1}$
j^{HH}_{2424}	$C^{H}_{24} \rightleftharpoons O^{H}_{24}$	$6.46532 \times 10^{7}\ \mu M^{-6}\ ms^{-1}$
j_{3132}	$C^{L}_{30} \rightleftharpoons C^{L}_{34}$	$5.01187\ \mu M^{-3}\ ms^{-1}$
j_{3334}	$C^{L}_{32} \rightleftharpoons C^{L}_{34}$	$2.00475 \times 10^{4}\ \mu M^{-7}\ ms^{-1}$
j_{0001}	$C^{L}_{00} \rightleftharpoons C^{I}_{04}$	$0.0033\ \mu M^{-1}\ ms^{-1}$
j_{0304}	$C^{L}_{00} \rightleftharpoons C^{I}_{04}$	$8.019 \times 10^{5}\ \mu M^{-4}\ ms^{-1}$

Superscripts are used to distinguish between different flux parameters that connect different pairs of states that have the same numbers of ligands bound. For example, in both transitions $C^{I}_{24} \rightleftharpoons O^{I}_{24}$ and $C^{H}_{24} \rightleftharpoons O^{H}_{24}$, C^{I}_{24} and C^{H}_{24} are bound to the same number of Ca^{2+} and $InsP_3R$ and so are O^{I}_{24} and O^{H}_{24}. However, the two transitions have different flux parameters

$$\frac{\partial b^{j}_{m}}{\partial t} = D_m \nabla^2_j b^{j}_{m} + k^{r}_{m}(B_m - b^{j}_{m}) - k^{f}_{m} c^{j} b^{j}_{m} \tag{3}$$

$$\frac{\partial b^{j}_{d}}{\partial t} = D_d \nabla^2_j b^{j}_{d} + k^{r}_{d}(B_d - b^{j}_{d}) - k^{f}_{d} c^{j} b^{j}_{d}. \tag{4}$$

In the above equations B_i is the total concentration, k^{f}_{i} the forward (binding) rate and k^{r}_{i} reverse (unbinding) rate for the various buffers with $i = s, m, d$. D_c, D_m and D_d are the diffusion coefficients for Ca^{2+}, mobile buffers and dye respectively. These evolution equations comprise an approximation analogous to the tight-binding model from solid state

physics in which the consumption of buffers in the vicinity of the j^{th} channel due to Ca^{2+} released by the i^{th} channel (with $i \neq j$) is neglected as the buffer consumed by a channel near its own pore is much higher than the buffer consumed by the same channel at the location of its neighbor [12]. As pointed out in [15], this may lead to underestimation of cytosolic Ca^{2+} concentration during the opening of channels and overestimation when all channels have closed, which makes this a crude approximation but not as crude as others have made in the field [16–18].

We consider a slow mobile buffer mimicking ethylene glycol tetraacetic acid (EGTA) and the fast mobile buffer 1,2-bis(o-aminophenoxy)ethane-N,N,N',N'-tetraacetic acid (BAPTA). The term 'slow' refers to the binding kinetics of the buffer, not its mobility. We simulate the propagation of Ca^{2+} and buffers throughout a homogeneous 3D cytosolic space using fixed boundary conditions where $\mathcal{C}_i = 50$ nM at the boundary. As presented in [15] these boundary conditions can be written in mathematical form as

$$\lim_{r_j \to 0} \left(-2\pi r_j^2 D_c \frac{\delta c^j}{\delta r_j} \right) = \sigma, \qquad c^j(R) = 50 \text{ nM}. \tag{5}$$

where $\sigma = I/(Z \times F)$ is the source strength and $R = 5$ μm is the radius of the simulating sphere. I, $Z = 2$ and F represent the Ca^{2+} current passing through the channel, valence of Ca^{2+} and Faraday's constant respectively. Previous studies have concluded that a single $InsP_3R$ channel releases a current of about 0.05–0.5 pA [8, 19, 20]. Throughout this manuscript we will assume a standard single-channel current of $I = 0.05$ pA when the channel is open, and zero otherwise.

The concentration of a given free buffer at the boundary of a sphere is fixed at its total concentration. For example, EGTA is fixed at 100 μM etc.

$J_j = \sigma/\delta V$ in (1) is the Ca^{2+} flux through the j^{th} channel when open, where δV is the volume of the hemisphere over the channel having a radius of 2.5 nm [21]. $J_j = 0$ when the channel is closed. The various parameters used in (1–4) are given in Table 4.

Table 4 Concentrations and rates

Quantity	Symbol	—	Numerical value	Reference
Resting Cytosolic Calcium	Ca_{rest}	=	50 nM	[22]
Stationary buffer	B_s	=	100 μM	[23, 24]
Dye Buffer	B_d	=	25, 40 μM	
EGTA	B_{EGTA}	=	0, 100 μM	
BAPTA	B_{BAPTA}	=	0, 50 μM	
Ca^{2+}	D_c	=	0.223 μm^2/ms	[25]
Dye	D_d	=	0.200 μm^2/ms	[26]
Mobile Buffers	D_m	=	0.200 μm^2/ms	[26]
Stationary Buffer	k_s^f	=	0.2 μM^2/ms	[22]
	k_s^r	=	$0.4/ms$	[22]
Dye Buffer	k_d^f	=	0.1 μM/ms	[22, 26]
	k_d^r	=	0.025/ms	[22, 26]
EGTA	k_{EGTA}^f	=	0.006 μM/ms	[22, 26]
	k_{EGTA}^r	=	0.001/ms	[22, 26]
BAPTA	k_{BAPTA}^f	=	0.8 μM/ms	[22, 26]
	k_{BAPTA}^r	=	0.2/ms	[22, 26]

The propagation of Ca^{2+} and buffers is simulated throughout a 3D cytosolic space. Considering the spherical symmetry around the channel, the Laplacian of Ca^{2+} and buffers in spherical coordinates is given as:

$$\nabla_j^2 X(r_j, t) = \frac{1}{r_j^2} \frac{\partial}{\partial r_j} \left(r_j^2 \frac{\partial X}{\partial r_j} \right) \tag{6}$$

where $X = c, b_m, b_d$.

The set of differential equations (1–6) was solved implicitly on a spherical volume of radius 5 μm with a spatial grid size of 5 nm using the Tridiagonal Matrix (TM) solver for each channel and the contribution of all channels was summed for the instantaneous Ca^{2+} concentration at a given point in space [12]. The idea is that we are simulating the dynamics of a puff-site that is far from the plasma membrane, in essence a single puff-site in a semi-infinite medium. Under the simulated conditions the Ca^{2+} concentration at 5 μm does not change significantly. Thus we use 5 μm as the radius of the simulated volume. Increasing the radius of the simulated volume does not make an appreciable difference. The assumption that each channel has its own reservoir of buffers converts the 3D problem into N 1D problems, where N is the total number of channels. In this case, we solve 10 1D problems each with 1000 grid points. Solving this problem numerically with a similar resolution in Cartesian coordinates, for example, would require about a billion grid points, a very demanding computational job where thousands of puffs have to be simulated to extract statistics.

Finally, the Ca^{2+} concentration at the location of each channel i, $\mathcal{C}_i$, is updated by adding the contributions from other channels in the cluster

$$\mathcal{C}_i = \sum_{j=1}^{10} c^j(r_{ij}) \tag{7}$$

where r_{ji} is the distance between channels i and j.

As we discussed in [12], this method is similar in spirit to the quasi-static approximation made by Nguyen et al. [16] where local Ca^{2+} experienced by channel i due to other channels was calculated as:

$$C_i = \sum\nolimits_{j=1}^{N} \frac{I_j e^{-r/\lambda}}{2\pi Dr}.$$

Here I_j, r, λ and D are the source amplitude of channel j, distance of channel j from channel i, buffer space constant and effective diffusion coefficient of Ca^{2+} respectively. $I_j = 0$ when channel j is closed (see also [17]). The approximation made by [16, 17] is binary; an open channel contributes $\frac{Ie^{-r/\lambda}}{2\pi Dr}$ while a closed channel makes no contribution to the overall Ca^{2+} profile. We relax the binary static approximation made in these two studies. When a channel first opens the contribution to the overall Ca^{2+} profile is approximately

$$\frac{Ie^{-r/\lambda}}{2\pi Dr}.$$

The contribution to the profile continues to evolve on a low time-scale. When an open channel first closes, its contribution to the overall profile rapidly drops to a low but nonzero level and then decays slowly to zero. Furthermore, when the first channel opens, the quasi-static approximation made by Nguyen et al. [16] fixes the first channel's contribution to the Ca^{2+} concentration at the second channel. In reality, the first channel's contribution to the Ca^{2+} concentration at the second channel will continue to increase as long as the

first channel is open. Our approximation tracks these time-dependent contributions of the channels to the Ca^{2+} profile.

Fluorescence signals representing Ca^{2+} time-traces recorded by Total Internal Reflection Fluorescence (TIRF) microscopy shown in Fig. 2 (top panels) are estimated by the procedure outlined in [12, 19].

In [10] we derived analytical expressions for the modal characteristics of a single channel as a function of ligand concentrations using the Markov chain model in Fig. 1. However, in the present situation where $\mathcal{C}_i$ changes dynamically during the evolution of blips and puffs we use the algorithm developed in [4] to characterize the modal behavior of individual channels in the cluster. A detailed description of the algorithm is given in [4] and [14] and

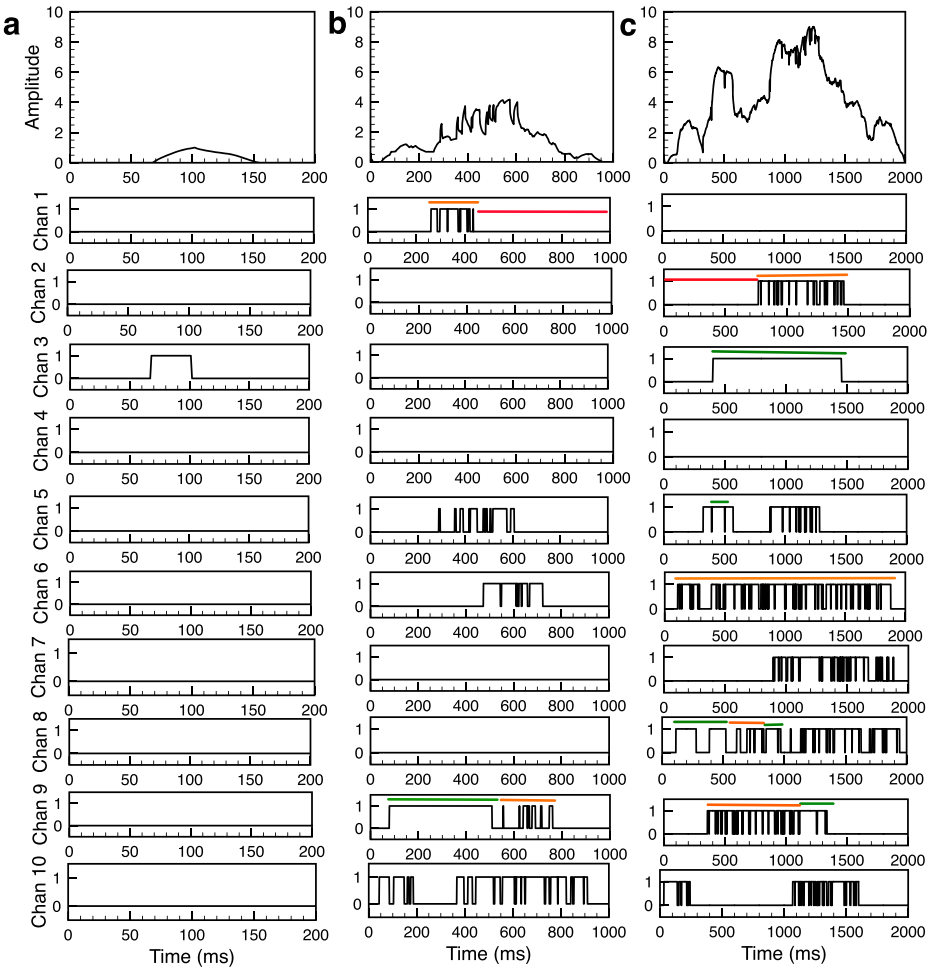

Fig. 2 Time series of an elementary Ca^{2+} event from the model. Example of blip (**a**), intermediate puff (**b**) and large puff (**c**). Top panels in (**a**), (**b**) and (**c**) show the fluorescence signal caused by Ca^{2+} released during the event followed by 10 panels showing the gating of all channels in the cluster. Examples of the three different modes are shown by the *lines* over time traces, where the *red, orange and green lines* represent the low, intermediate and high mode respectively. $InsP_3 = 100$ nM, $B_s = 100\ \mu$M, $B_d = 25\ \mu$M, $B_{EGTA} = 100\ \mu$M, and $B_{BAPTA} = 0\ \mu$M

briefly described here. The channel makes a modal transition when two or more consecutive burst-terminating gaps (t_g) have $t_g \leq 200$ ms following at least one gap with $t_g > 200$ ms but not when just one gap has $t_g \leq 200$ ms. However, a modal transition is recognized when a single burst-terminating gap with $t_g > 200$ ms follows one or several consecutive gaps with $t_g \leq 200$ ms. Similarly, a modal transition is registered when a single channel burst has burst duration $t_b > 100$ ms following a series of bursts with $t_b \leq 100$ ms: a modal transition is only registered when two consecutive channel bursts have $t_b \leq 100$ ms following a series of bursts with $t_b > 100$ ms. After the modal transitions are identified, the channel is then classified as being in the I mode if $t_g \leq 200$ ms and $t_b \leq 100$ ms; in the H mode if $t_g \leq 200$ ms and $t_b > 100$ ms; and in the L mode if $t_g > 200$ ms and $t_b \leq 100$ ms.

We remark that although the single channel model shown in Fig. 1 does not include an open state when $InsP_3R$ gates are in the L mode, the modal characterization algorithm discussed in the previous paragraph will detect an open state in the L mode when the criterion for the L mode is met while running the algorithm on the time traces obtained for each channel during blips and puffs. We would like to mention that the modal statistics can also be derived directly without using the algorithm described above by recording all twelve states for each channel as a function of time in the simulation, in which case one would not see an open state when a channel is gating in the L mode.

3 Results

The stochastic scheme outlined in the previous section allows us to simulate elementary Ca^{2+} release events. Examples of Ca^{2+} blips and puffs given by the model are shown in Fig. 2. The top panels in Fig. 2a, b, c show the event amplitudes in terms of fluorescence signal caused by Ca^{2+} release through the cluster, followed by 10 panels showing the gating of all 10 channels during the event. The blip shown in Fig. 2a is caused by the brief single opening of channel 3 in the cluster while all other channels remain closed. Thus all channels gate in low mode during the blip. During the small puff, five channels open, exhibiting short bursts that are reminiscent of intermediate mode (Fig. 2b). Only channel 9 briefly exhibits high mode followed by intermediate mode. The remaining five channels are in low mode. Eight out of ten channels open simultaneously during the longer puff (Fig. 2c). All open channels, except channel 6, spend some fraction of time in the high mode. Thus it is evident from Fig. 2 that, as the time spent by the channels in the intermediate and high modes increases, the size of the elementary Ca^{2+} release event increases.

To analyze the single channel behavior during Ca^{2+} signals of different spatiotemporal scales, we increase the concentration of $InsP_3$. In experiments, modest $InsP_3$ concentration leads to spatially confined Ca^{2+} blips, confined Ca^{2+} blips and puffs [5, 27], while larger $InsP_3R$ stimulus causes whole cell waves or oscillations [28–30]. Bearing in mind this transition from blips to puffs and waves as a function of $InsP_3$ concentration, we vary $InsP_3$ in the model from 25 nM to 1 μM and plot the average statistics of elementary Ca^{2+} events along with the modal characteristics of $InsP_3R$ as shown in Fig. 3. For a given $InsP_3R$ concentration, we run the simulation for 1000 seconds (real time) and compute the average statistical properties of blips and puffs based on several hundred events. Both the average amplitude defined as the maximum number of simultaneously open channels during the event (Fig. 3a, open triangles) and the duration (Fig. 3a, filled triangles) of the blips and puffs combined increase as we increase $InsP_3$ concentration. The cluster particularly leads to larger amplitude (Fig. 3a, open circles) and longer duration (Fig. 3a, filled circles) puffs for high $InsP_3$ concentration that would most likely recruit other puff sites leading to

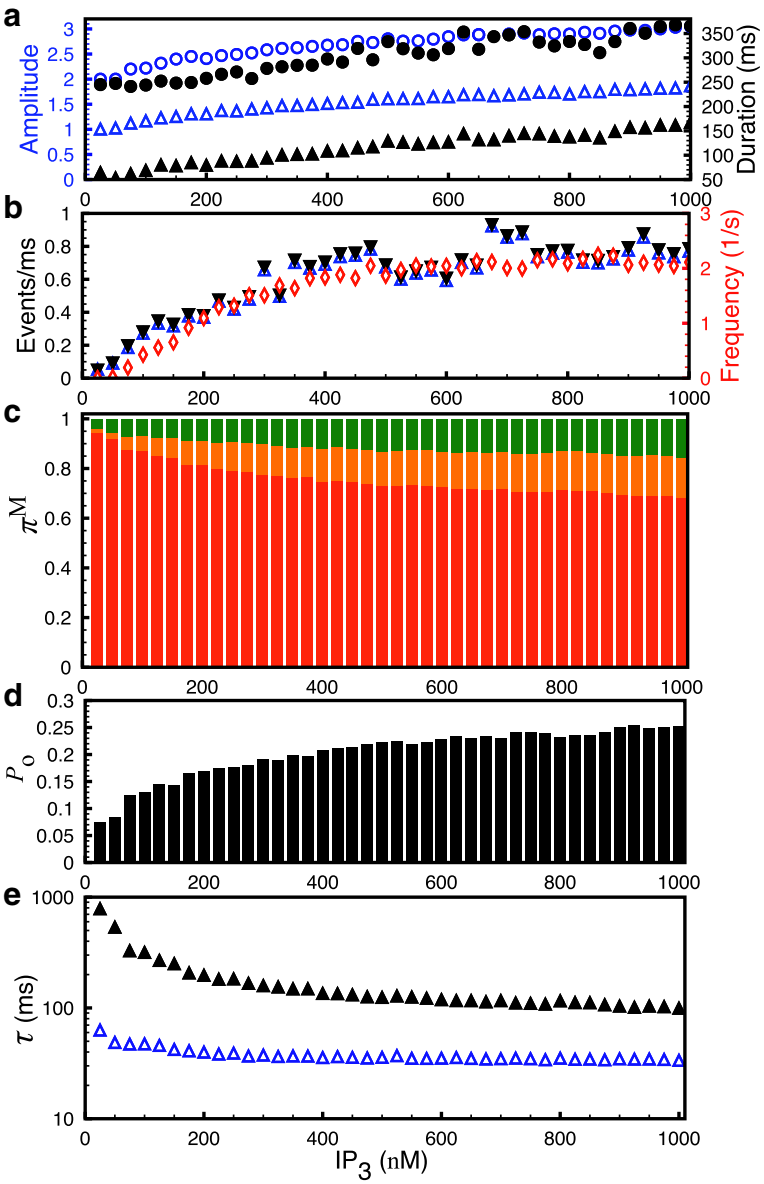

Fig. 3 Statistics of elementary Ca^{2+} release events and single channel modal properties as a function of $InsP_3$ concentration. **a** Average amplitude of blips and puffs combined (*empty triangles*), puffs only (*empty circles*) and duration of blips and puffs combined (*filled triangles*), puffs only (*filled circles*). **b** mean channel openings (*empty triangles*) and closings (*filled triangles*) per millisecond during the puffs and frequency of puffs (*empty diamonds*). **c** Prevalence, π^M, of the three modes. The superscript M is L for low mode (*red*), I for intermediate mode (*orange*) and H for high mode (*green*). **d** P_o and **e** τ_o (*open triangles*) and τ_c (*filled triangles*) of $InsP_3R$. $B_s = 100\ \mu$M, $B_d = 25\ \mu$M, $B_{EGTA} = 100\ \mu$M, and $B_{BAPTA} = 0\ \mu$M

whole cell waves and oscillations [29, 31]. Similarly, the average rate of channel openings (Fig. 3b, open triangles) and closings during the events (Fig. 3b, filled triangles) increases

as a function of $InsP_3$ concentration. The average rate of channel openings and closings was calculated by counting the total number of channels that opened or closed during the event and dividing the number by the duration of that event. Finally, the openings and closings per millisecond were averaged for all events. The frequency of puffs saturates after an initial rise as a function of $InsP_3$ concentration indicating a larger fraction of events with larger amplitude and longer life-time (Fig. 3b, diamonds). The change in the average rate of channel openings and closings indicates a change in the gating behavior or activity mode of $InsP_3R$ and shows a relationship with the average statistics of elementary Ca^{2+} release events.

Figure 3c shows the prevalences (the probability of the channel gating in a given mode) of three modes, π^M, defined as the normalized probability that the channel is gating in a given mode. The prevalence of intermediate and high modes increases as we increase $InsP_3R$ concentration, indicating a direct link between the modal behavior of the channel and Ca^{2+} patterning. The P_o, mean open (τ_o), and closed (τ_c) time of the channel are the other measures of the modal behavior of the channel. The average P_o of the channels in the cluster increases from a value representative of low mode to that higher than the intermediate mode (Fig. 3d). τ_o (Fig. 3e, open triangles) remains almost constant while τ_c (Fig. 3e, filled triangles) decreases by an order of magnitude as we increase $InsP_3$ concentration. The behavior of τ_o and τ_c shown here is again an indication of the change in the modal behavior of the channel. This is reminiscent of experimental data where τ_c of the channel was observed to

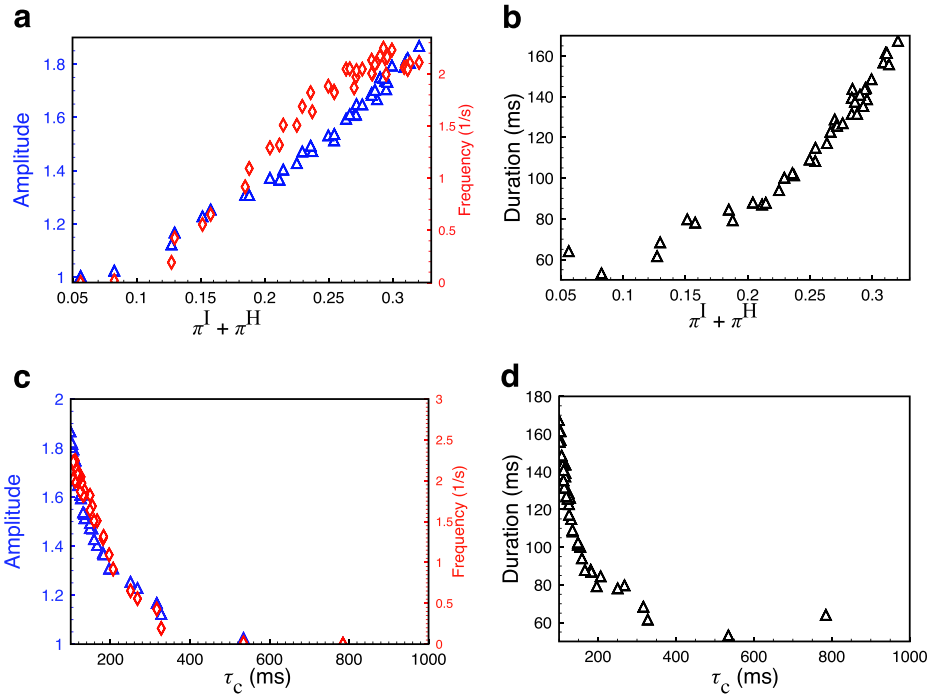

Fig. 4 Average statistics of elementary Ca^{2+} release events vary as a function of single channel modal characteristics. **a** Average amplitude (*triangles*), frequency (*diamonds*) and **b** mean duration of puffs as a function of total prevalence of I and H modes. **c** Average amplitude (*triangles*) and frequency (*diamonds*) and **d** mean duration of puffs (*triangles*) versus the mean closed time of a single channel. $B_s = 100\ \mu$M, $B_d = 25\ \mu$M, $B_{EGTA} = 100\ \mu$M and $B_{BAPTA} = 0\ \mu$M

drop from over a second for the low mode to less than 100 ms in intermediate and high modes [4, 14]. The τ_o on the other hand remained constant within a few milliseconds.

To further illustrate the relationship between Ca^{2+} patterning and the gating behavior of a single channel, we plot the average characteristics of elementary Ca^{2+} release events as a function of modal statistics (Fig. 4). The average amplitude, frequency and duration of blips and puffs increase as the total prevalence of intermediate and high modes increases (Fig. 4a, b). The average amplitude, frequency (Fig. 4c), and average life-time of puffs (Fig. 4d) decrease exponentially as a function of τ_c of a single channel.

So far we have been exploring the dependence of average statistics of elementary Ca^{2+} events on the modal characteristics of individual channels. To explore a more one-to-one relation of puffs with the modal behavior, we binned thousands of events according to their

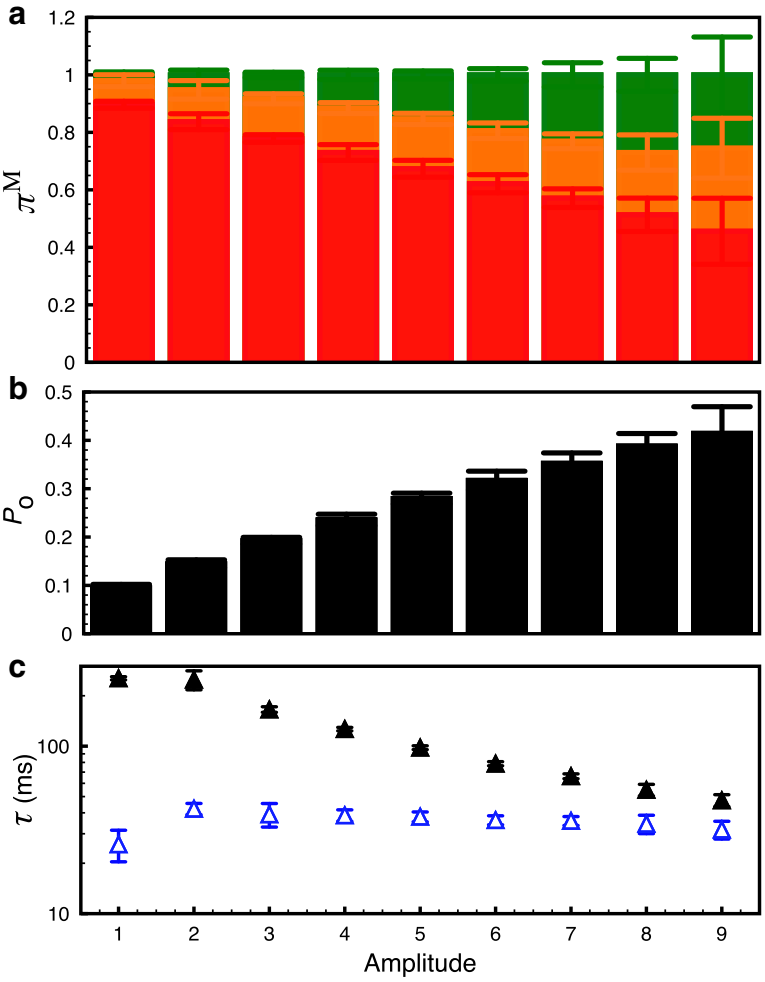

Fig. 5 Modal properties of channels during events with different amplitudes. **a** Prevalence of low (*red*), intermediate (*orange*) and high (*green*) mode during puffs with different average amplitudes. **b** P_o and **c** τ_o (*open triangles*), τ_c (*filled triangles*) of $InsP_3R$ during puffs with different average amplitudes. $B_s = 100\ \mu M$, $B_d = 25\ \mu M$, $B_{EGTA} = 100\ \mu M$, and $B_{BAPTA} = 0\ \mu M$

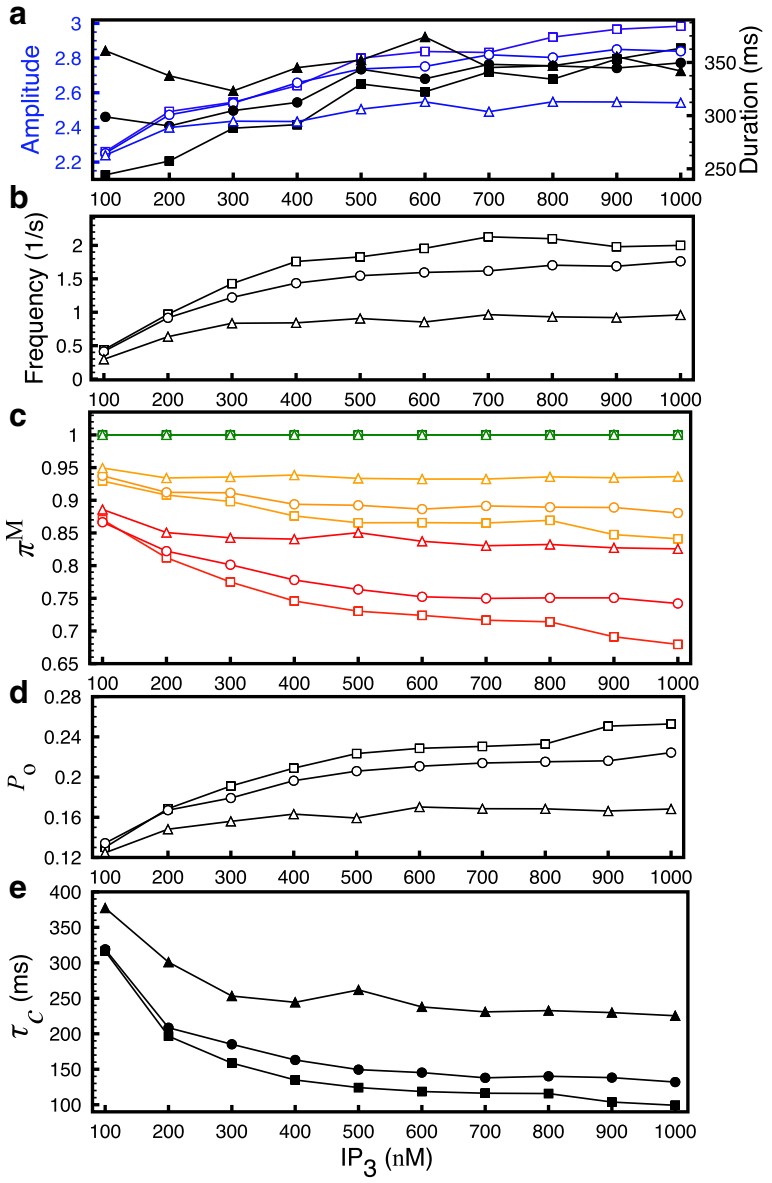

Fig. 6 Statistics of elementary Ca^{2+} release events and single channel modal properties as a function of $InsP_3$ concentration in the presence of different buffer concentrations. **a** Average amplitude (*empty symbols*) and duration of puffs (*filled symbols*), **b** frequency of puffs and **c** prevalence π^M of the three modes. The superscript M is L for low mode (*red*), I for intermediate mode (*orange*) and H for high mode (*green*). **d** P_o and **e** τ_c of $InsP_3R$. *Squares, circles* and *triangles* are for control simulations from Fig. 3 ($B_s = 100$ μM, $B_d = 25$ μM, $B_{EGTA} = 100$ μM, and $B_{BAPTA} = 0$ μM), ($B_s = 100$ μM, $B_d = 40$ μM, $B_{EGTA} = 100$ μM, and $B_{BAPTA} = 0$ μM) and ($B_s = 100$ μM, $B_d = 25$ μM, $B_{EGTA} = 100$ μM and $B_{BAPTA} = 50$ μM) respectively

amplitude and computed the modal characteristics of all channels for each bin. Note that each bin contains many events having the same amplitude. Figure 5 shows the result of these

simulations. A higher probability of low mode leads to blips; however, as the probability of intermediate and high modes increases, the amplitude of events increases. When the individual channels have more than 50% probability of being in the intermediate and/or high modes, on average nine out of ten channels in the cluster open during a puff, resulting in very large Ca^{2+} events that would most likely recruit neighboring puff sites, thus triggering global Ca^{2+} signals (Fig. 5a). The P_o of channels rise from the value close to the low mode to the range between intermediate and high modes (Fig. 5b). The τ_o remains constant except for an early rise as the amplitude increases (open triangles, Fig. 5c). The τ_c of the channel drops significantly, indicating a shift in the gating of channels from low to intermediate and high modes resulting in bigger puffs (filled triangles, Fig. 5c).

Next, we evaluate the effect of various buffers on the gating properties of a single $InsP_3R$ inside the puff site and the statistics of puffs. We change the concentration of a single buffer at a time and compare our results with those from the control simulations discussed above ($B_s = 100\ \mu$M, $B_d = 25\ \mu$M, $B_{EGTA} = 100\ \mu$M and $B_{BAPTA} = 0\ \mu$M) (Fig. 6, squares). Increasing B_d from 25 μM to 40 μM (Fig. 6, circles) and B_{BAPTA} from 0 μM to 50 μM (Fig. 6, triangles) increases the duration of puffs (Fig. 6a, filled symbols), especially at lower $InsP_3$ concentration. The average amplitude of puffs at smaller $InsP_3$ concentration decreases slightly but has a significant drop at high $InsP_3$ concentration (Fig. 6a, open symbols). Thus increasing both dye and BAPTA lead to smaller puffs with longer lifetimes. The frequency of puffs also decreases significantly (Fig. 6b). This behavior of puffs can be explained by the change in the modal behavior of the channels where the prevalence of low mode increases and that of the high mode decreases as we increase dye and BAPTA concentrations (Fig. 6c). The prevalence of the intermediate mode on the other hand decreases slightly as we increase dye and BAPTA concentrations. Notice that the prevalence of high mode in (Fig. 6c) is given by the difference in the green and orange lines, while that of intermediate mode is given by the difference between the red and orange lines for a given parameter set (as in Fig. 3c). Consistent with our conclusion from Fig. 3, the change in modal behavior results in the decreased P_o (Fig. 6d) and increased τ_c (Fig. 6e) of the channel. The mean open time of the channel does not change significantly and is not shown here. Changing B_{EGTA} from 100 μM to 0 μM did not change the modal behavior of the single channel and the statistics of the puffs and is therefore not shown here.

4 Conclusions

The opening of a single $InsP_3R$, the nearly simultaneous opening of more than one $InsP_3R$ inside a single channel cluster, and the coordinated activation of multiple clusters on the intracellular stores underlie the spatiotemporal patterning of Ca^{2+} transients essential for regulating numerous highly specific cellular functions [1]. The gating behavior of individual channels in conjunction with the cluster architecture, inter-cluster spacing and buffered and free Ca^{2+} diffusion play a role in shaping these spatiotemporal scales. However, the cluster architecture and inter-cluster spacing do not change significantly over the time scale of these events [32]. Thus the gating behavior of the channel seems to be the main driving force for spatiotemporal patterning of Ca^{2+} signals. Despite many years of research, the limitations in experimental tools impair our ability to elucidate the single channel behavior during Ca^{2+} signals of different scales, which is the subject of this study.

We show that as the average channel behavior changes from gating in the low mode to gating in the intermediate and high modes the amplitude and duration of Ca^{2+} signals increase (Figs. 2 and 3). In fact, the mean amplitude, duration and frequency of Ca^{2+} signals

all increase linearly as functions of total prevalence of intermediate and high modes (Fig. 4a, b). Channels gating predominantly in low mode lead to blips (Figs. 2a and 5). The size of the events increases from blips to small puffs as the probability of the channel gating in the intermediate and high mode begins to rise (Figs. 2b, c, and 5). When the prevalence of intermediate and/or high modes is very high, the cluster gives rise to very large puffs. For example, if the combined prevalence of intermediate and high modes is more than 50%, the puff site generates puffs where on average nine out of ten channels are open during the puff (Fig. 5). Although we do not simulate whole-cell Ca^{2+} waves and oscillations, these events with large amplitude and longer duration occurring at high frequency would most likely trigger global Ca^{2+} signals [31].

Consistent with the observations during single channel patch-clamp experiments [4] and recent modeling study [14], our results show that the transition of the channel behavior from gating predominantly in low mode during small events to gating in the intermediate and high modes during large events is due to the significant decrease in τ_c with a slight increase in τ_o of the channel (Figs. 3e and 5). Thus, the gating properties of $InsP_3R$ leading to Ca^{2+} signals of different scales boil down to the change in τ_c of the channel.

It is worth noticing that our single channel model developed in Ref. [10] is not the only model that is driven by both stationary and nonstationary data on $InsP_3R$ that also represents the modal behavior of the channel. Neither is ours the first instance where a model representing the modal behavior of $InsP_3R$ is used for simulating puffs. Siekmann et al. developed a six-state model incorporating the modal behavior of the channel [33] that was shown to reproduce the statistics of puffs [34] and whole-cell oscillations [35]. Simplifying the six states to a two-state model by getting rid of the intra-modal structure and using the two versions of the model, Siekmann et al. [36] demonstrated that the fundamental process governing the generation of Ca^{2+} puffs and oscillations is primarily controlled by the inter-modal structure, not the intra-modal structure. This conclusion is in line with our observations where we found a direct relationship between the prevalence of the three modes and puff characteristics. Moreover, our study for the first time quantitatively relates the modal characteristics of $InsP_3R$ to the generation of Ca^{2+} signals at different spatiotemporal scales.

Acknowledgments This work was supported by a start-up grant from the College of Arts and Sciences at the University of South Florida awarded to GU and National Institute of Health (NIH) grant no. 5R01HL105239 and 5U01HL116321 (AU). We would like to thank the IT department at the University of South Florida for providing the computational resources and help with simulations.

References

1. Berridge, M.J., Lipp, P., Bootman, M.D.: The versatility and universality of calcium signalling. Nat. Rev. Mol. Cell Biol. **1**(1), 11–21 (2000)
2. Mak, D.O.D., McBride, S., Foskett, K.J.: IP_3 activation of IP_3R Ca^{2+} channel by ligand tuning of Ca^{2+} inhibition. Proc. Natl. Acad. Sci. USA **95**(26), 15,821–15,825 (1998)
3. Mak, D.O.D., McBride, S., Foskett, K.J.: Spontaneous channel activity of the IP_3R. Application of allosteric modeling to Ca^{2+} and IP_3 regulation of IP_3R single-channel gating. J. Gen. Physiol. **122**(5), 583–603 (2003)
4. Ionescu, L., White, C., Cheung, K.H., Shuai, J., Parker, I., Pearson, J.E., Foskett, K.J., Mak, D.O.D.: Mode switching is the major mechanism of ligand regulation of IP_3R Ca^{2+} release channels. J. Gen. Physiol. **130**(6), 631–645 (2007)
5. Smith, I.F., Parker, I.: Imaging the quantal substructure of single IP_3R channel activity during Ca^{2+} puffs in intact mammalian cells. Proc. Natl. Acad. Sci. USA **106**(15), 6404–6409 (2009). doi:10.1073/pnas.0810799106

6. Parker, I., Smith, I.: Recording single-channel activity of IP_3Rs in intact cells with a microscope, not a patch clamp. J. Gen. Physiol. **136**(2), 119–127 (2010)
7. Shuai, J., Rose, H., Parker, I.: The number and spatial distribution of IP_3Rs underlying Ca^{2+} puffs in *Xenopus* oocytes. Biophys. J. **91**(11), 4033–4044 (2006)
8. Bruno, L., Solovey, G., Ventura, A., Dargan, S., Dawson, S.: Quantifying Ca^{2+} fluxes underlying Ca^{2+} puffs in *Xenopus laevis* oocytes. Cell Calcium **47**(3), 273–286 (2010)
9. Mak, D.O.D., Pearson, J.E., Cheung, K.H., Datta, S., Fernandez-Mongil, M., Foskett, K.J.: Rapid ligand-regulated gating kinetics of single IP_3R Ca^{2+} release channels. EMBO Rep. **8**, 1044–1051 (2007)
10. Ullah, G., Mak, D.O.D., Pearson, J.E.: A data-driven model of a modal gated ion channel: the inositol 1, 4, 5-trisphosphate receptor in insect Sf9 cells. J. Gen. Physiol. **140**(2), 159–173 (2012)
11. Vais, H., Foskett, J.K., Ullah, G., Pearson, J.E., Mak, D.O.D.: Permeant calcium ion feed-through regulation of single inositol 1, 4, 5-trisphosphate receptor channel gating. J. Gen. Physiol. **140**(6), 697–716 (2012)
12. Ullah, G., Parker, I., Mak, D.O.D., Pearson, J.E.: Multi-scale data-driven modeling and observation of calcium puffs. Cell Calcium **52**(2), 152–160 (2012)
13. Ullah, G., Jung, P.: Modeling the statistics of elementary Ca^{2+} release events. Biophys. J. **90**(10), 3485–3495 (2006)
14. Mak, D.O.D., Cheung, K.H., Toglia, P., Foskett, J.K., Ullah, G.: Analyzing and quantifying the gain-of-function enhancement of IP_3 receptor gating by familial Alzheimer's disease-causing mutants in presenilins. PLoS Comput Biol **11**(10), e1004529 (2015)
15. Rüdiger, S.: Stochastic models of intracellular calcium signals. Phys. Rep. **534**(2), 39–87 (2014)
16. Nguyen, V., Mathias, R., Smith, G.: A stochastic automata network descriptor for Markov chain models of instantaneously coupled intracellular Ca^{2+} channels. Bull. Math. Biol. **67**(3), 393–432 (2005)
17. Neher, E.: Vesicle pools and Ca^{2+} microdomains: new tools for understanding their roles in neurotransmitter release. Neuron **20**, 389–399 (1998)
18. Rüdiger, S., Shuai, J.W., Sokolov, I.M.: Law of mass action, detailed balance, and the modeling of Ca^{2+} puffs. Phys. Rev. Lett. **105**(4), 048103 (2010). doi:10.1103/PhysRevLett.105.048103
19. Shuai, J., Parker, I.: Optical single-channel recording by imaging Ca^{2+} flux through individual ion channels: theoretical considerations and limits to resolution. Cell Calcium **37**(4), 283–299 (2005)
20. Vais, H., Foskett, K.J., Mak, D.O.D.: Unitary Ca^{2+} current through recombinant type 3 IP_3 receptor channels under physiological ionic conditions **136**(6), 687–700 (2010). doi:10.1085/jgp.201010513
21. Shuai, J., Pearson, J., Foskett, K.J., Mak, D.O.D., Parker, I.: A kinetic model of single and clustered IP_3 receptors in the absence of Ca^{2+} feedback. Biophys. J. **93**(4), 1151–1162 (2007)
22. Falcke, M.: Reading the patterns in living cells-the physics of Ca^{2+} signaling. Adv. Phy. **53**(3), 255–440 (2004)
23. Neher, E., Augustine, G.: Ca^{2+} gradients and buffers in bovine chromaffin cells. J. Physiol. **450**(1), 273–301 (1992)
24. Zhou, Z., Neher, E.: Mobile and immobile Ca^{2+} buffers in bovine adrenal chromaffin cells. J. Physiol. **469**(1), 245–273 (1993)
25. Allbritton, N., Meyer, T., Stryer, L.: Range of messenger action of Ca^{2+} ion and IP_3. Genes Dev. **4**, 1753 (1990)
26. Dargan, S., Parker, I.: Buffer kinetics shape the spatiotemporal patterns of IP_3-evoked Ca^{2+} signals. J. Physiol. **553**(3), 775–788 (2003)
27. Sun, X.P., Callamaras, N., Marchant, J.S., Parker, I.: A continuum of $InsP_3$-mediated elementary Ca^{2+} signalling events in *Xenopus* oocytes. J. Physiol. **509**(1), 67–80 (1998)
28. Callamaras, N., Parker, I.: Phasic characteristic of elementary Ca^{2+} release sites underlies quantal responses to IP_3. EMBO J. **19**(14), 3608–3617 (2000)
29. Marchant, J.S., Parker, I.: Role of elementary Ca^{2+} puffs in generating repetitive Ca^{2+} oscillations. EMBO J. **20**(1-2), 65–76 (2001)
30. Dupont, G., Combettes, L., Bird, G.S., Putney, J.W.: Calcium oscillations. Cold Spring Harb. Perspect. Biol. **3**(3), a004226 (2011)
31. Rückl, M., Parker, I., Marchant, J.S., Nagaiah, C., Johenning, F.W., Rüdiger, S.: Modulation of elementary calcium release mediates a transition from puffs to waves in an IP_3R cluster model. PLoS Comput. Biol. **11**(1), e1003965 (2015)
32. Smith, I.F., Swaminathan, D., Dickinson, G.D., Parker, I.: Single-molecule tracking of inositol trisphosphate receptors reveals different motilities and distributions. Biophys. J. **107**(4), 834–845 (2014)
33. Siekmann, I., Wagner, L.E., Yule, D., Crampin, E.J., Sneyd, J.: A kinetic model for type I and II IP_3R accounting for mode changes. Biophys. J. **103**(4), 658–668 (2012)

34. Cao, P., Donovan, G., Falcke, M., Sneyd, J.: A stochastic model of calcium puffs based on single-channel data. Biophys. J. **105**(5), 1133–1142 (2013)
35. Cao, P., Tan, X., Donovan, G., Sanderson, M.J., Sneyd, J.: A deterministic model predicts the properties of stochastic calcium oscillations in airway smooth muscle cells. PLoS Comput. Biol. **10**(8), e1003783 (2014)
36. Siekmann, I., Cao, P., Sneyd, J., Crampin, E.J.: Data-driven modelling of the inositol trisphosphate receptor (ipr) and its role in calcium induced calcium release (CICR). arXiv:1507.06064 (2015)